

RESEARCH ARTICLE

A framework for isogeometric-analysis-based optimization of wind turbine blade structures

Austin J. Herrema*¹ | Josef Kiendl² | Ming-Chen Hsu¹

¹Department of Mechanical Engineering, Iowa State University, 2025 Black Engineering, Ames, Iowa 50011, USA

²Department of Marine Technology, Norwegian University of Science and Technology, O. Nielsens veg 10, 7052 Trondheim, Norway

Correspondence

*Austin J. Herrema, Department of Mechanical Engineering, Iowa State University, 2025 Black Engineering, Ames, Iowa 50011, USA. Email: austin.j.he@gmail.com

Summary

Early-stage wind turbine blade design usually relies heavily on low-fidelity structural models; high-fidelity, finite-element-based structural analyses are reserved for later design stages because of their complex workflows and high computational expense. Yet, high-fidelity structural analyses often provide design-governing feedback such as buckling load factors. Mitigation of the issues of workflow complexity and computational expense would allow designers to utilize high-fidelity feedback earlier, more easily, and more often in the design process. Thus, a blade analysis framework that employs isogeometric analysis (IGA), a simulation method that overcomes many of the aforementioned drawbacks associated with traditional finite element analysis (FEA), is presented. IGA directly utilizes the mathematical models generated by computer-aided design (CAD) software, requiring less user interaction and no conversion of parametric geometries to finite element meshes. Furthermore, IGA tends to have superior per-degree-of-freedom accuracy compared with traditional FEA. Issues unique to IGA in the context of wind turbine blade design, such as coupling of thin-shell components, are addressed, and a design approach that combines reduced-order aeroelastic analysis with IGA is outlined. Aeroelastic analysis is used to efficiently provide dynamic kinematic data for a wide range of wind load cases, while IGA is used to perform buckling analysis. The value of incorporating high-fidelity analysis feedback into blade design is demonstrated through optimization of the NREL/SNL 5 MW wind turbine blade. A variety of potential designs are produced with reduced blade mass and material cost, and IGA-based buckling analysis is shown to provide design-governing constraint information.

KEYWORDS:

blade design; optimization; finite element; isogeometric analysis; buckling; NREL/SNL 5 MW

1 | INTRODUCTION

The trend of increasing wind turbine blade length is ultimately driven by the pursuit of cheaper wind energy through larger swept areas. However, under some basic assumptions, it can be shown that while rotor power increase is related to rotor size through a quadratic relationship, rotor weight is related to rotor size through a cubic relationship.¹ This is known as the cube-square law and it suggests significant challenges in the design of larger blades, especially because cost-effectiveness is a priority. Although the cube-square law appears to have been overcome in practice through a variety of design methods,² increasing blade length nevertheless entails considerable structural design challenges. In particular, it has been suggested that blade buckling, especially with regard to nonlinear effects, is of concern for longer blades.³⁻⁷

Wind turbine blade design typically relies heavily on computationally efficient, reduced-order aerodynamic and structural models, especially in the early stages of blade design. This is a sensible approach given a vast design space, the large number of design iterations typically performed, and

the ample accuracy of many reduced-order models. The value of reduced-order approaches can be especially realized in the context of optimization.⁸⁻¹⁵ Some types of analyses, however, are more difficult to perform reliably using reduced-order models. Thus, higher-fidelity finite element analysis (FEA), including both shell and solid FEA, is typically employed in the later design stages to evaluate, for example, buckling load factors as required by design standards such as the IEC 61400.¹⁶ Because blades are often optimized without taking this accurate buckling feedback into account, late-stage FEA can reveal design flaws that trigger additional, laborious design iteration. Notably, the focus during these iterations usually shifts away from blade optimality and towards satisfaction of design standards. To address these issues, various creative design approaches can be employed. For example, Bottasso et al.¹⁷ constructed an optimization framework that employs multiple levels of fidelity. Regardless of the design approach used, however, the computational cost and labor associated with traditional FEA have the potential to be prohibitive. Thus, numerous design approaches stand to benefit from improved high-fidelity structural analysis workflows and methodologies.

The present work therefore outlines a framework for isogeometric analysis (IGA)-based design and optimization of wind turbine blade structures. IGA was first introduced by Hughes et al.¹⁸ and is based on the idea that the smooth, parametric functions used in computer-aided design (CAD) can also be used as finite element basis functions, eliminating the need for extra mesh generation. IGA is therefore capable of effectively uniting design and analysis paradigms, employing a single model for all such activities. This can ultimately reduce designer labor and requisite user interaction. IGA has also been shown to feature significantly improved per-degree-of-freedom accuracy relative to traditional FEA in many cases.^{19,20} Past wind turbine and wind turbine blade simulations have employed IGA,²¹⁻³² but none of these efforts have utilized IGA for the purposes of iterative blade design. The present framework enables IGA-based wind turbine blade design through a variety of unique approaches and developments presented herein. Furthermore, the framework is demonstrated through the modeling, analysis, and optimization of the NREL/SNL 5 MW reference blade design.

This paper is outlined as follows. The salient theoretical and technical aspects of the presented framework for isogeometric analysis of wind turbine blades are described in Section 2. In Section 3, the details of the reference 5 MW blade model are described, and the IGA-based model is presented and verified. Additionally, mesh convergence studies are performed and, where possible, the results are compared with results obtained using traditional FEA. In Section 4, the 5 MW blade design is optimized using a combination of reduced-order aeroelastic analyses and IGA-based buckling analysis. Lastly, Section 5 presents a variety of conclusions based on construction and employment of the IGA-based framework for blade design.

2 | FRAMEWORK FOR ISOGEOMETRIC ANALYSIS OF WIND TURBINE BLADES

2.1 | Isogeometric analysis fundamentals

Typical FEA methods rely on networks of interpolants (i.e. finite elements) to represent a solution field. These networks generally consist of nodes, at which the solution of interest is directly represented, and elements, over which the solution field is represented by predefined functions. Correspondingly, geometries in FEA are represented by finite element meshes comprised of, for example, linear triangular elements. Alternatively, CAD systems typically employ a variety of analytic or parametric functions, such as splines, for advanced geometry representation, visualization and manipulation. For the engineering designer utilizing both CAD and computer-aided engineering (CAE), these unique geometric paradigms entail the management of separate, but necessarily related, geometry descriptions. This can lead to a significant amount of manual labor for the design engineer.³³

The core recognition of Hughes et al.¹⁸ was that the parametric functions used by CAD systems to represent geometry can also be used to represent the solution fields of partial differential equations. For example, if an object is modeled geometrically using non-uniform rational B-splines (NURBS), which are employed in this work, the solution field can readily be represented using the exact same set of NURBS functions. This approach entails the significant practical advantage of needing to maintain only one geometry description throughout design and analysis. In addition to this, NURBS basis functions have a number of properties making them useful for analysis, including partition of unity and non-negativity. The partition of unity property indicates that, the sum of the values of all basis functions at any parametric location is equal to one. The property of non-negativity indicates that the value of any basis function is always greater than or equal to zero. The technical value of these properties is explored in detail by Hughes et al.¹⁸

Given a scalar parametric variable u , a B-spline curve is defined by a set of non-interpolated control points, \mathbf{P}_i , $i = 1, \dots, n$; degree, p ; and a knot vector, $\Xi = [\xi_1, \xi_2, \dots, \xi_{n+p+1}]$, which is a set of scalar parametric coordinates dividing the curve into segments over which distinct sets of basis functions have influence. The basis functions are defined by the Cox-deBoor recursion formula.³⁴ For degree $p = 0$,

$$N_{i,0}(\xi) = \begin{cases} 1 & \text{if } \xi_i \leq \xi < \xi_{i+1}, \\ 0 & \text{otherwise,} \end{cases} \quad (1)$$

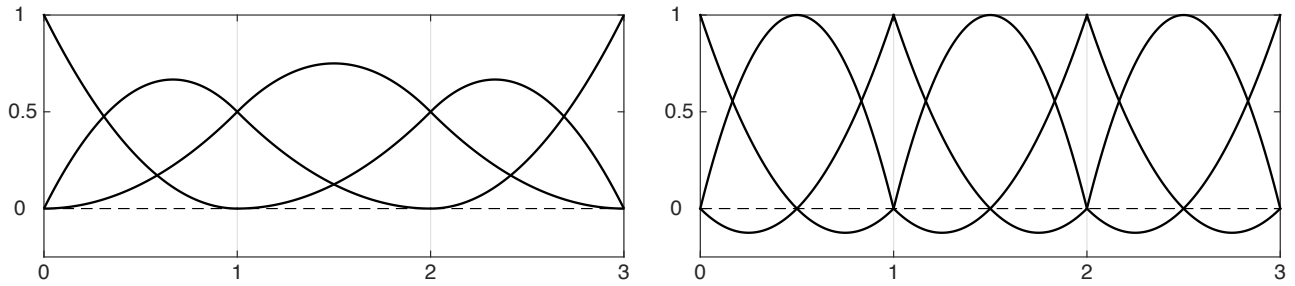


FIGURE 1 Quadratic NURBS (left) and Lagrange (right) basis functions shown over three elements.

and for degree $p \geq 1$,

$$N_{i,p}(\xi) = \frac{\xi - \xi_i}{\xi_{i+p} - \xi_i} N_{i,p-1}(\xi) + \frac{\xi_{i+p+1} - \xi}{\xi_{i+p+1} - \xi_{i+1}} N_{i+1,p-1}(\xi). \quad (2)$$

While rational B-splines are sufficient for representing many shapes, they are not capable of perfectly representing conic sections. Thus, B-spline basis functions can be further generalized to define NURBS entities. For each of the n control points, \mathbf{P}_i , a weight, w_i , is assigned. These weights are used to describe the relative strength of influence of a basis function, in effect defining new, rational basis functions:

$$R_i^p(\xi) = \frac{N_{i,p}(\xi) w_i}{\sum_{j=0}^n N_{j,p}(\xi) w_j}. \quad (3)$$

A NURBS curve can therefore be defined as a linear combination of the n basis functions and n control points:

$$\mathbf{C}(\xi) = \sum_{i=0}^n R_i^p(\xi) \mathbf{P}_i. \quad (4)$$

For a net of $m \times n$ control points, $\mathbf{P}_{i,j}$, and weights, $w_{i,j}$, and with the introduction of a second parametric direction, η ; associated knot vector, \mathcal{H} ; degree, q ; and set of basis functions, $N_{j,q}(\eta)$; a similar approach can be used to define bi-directional rational basis functions and NURBS surfaces:

$$R_{i,j}^{p,q}(\xi, \eta) = \frac{N_{i,p}(\xi) N_{j,q}(\eta) w_{i,j}}{\sum_{k=0}^n \sum_{l=0}^m N_{k,p}(\xi) N_{l,q}(\eta) w_{k,l}}, \quad (5)$$

$$\mathbf{S}(\xi, \eta) = \sum_{i=0}^n \sum_{j=0}^m R_{i,j}^{p,q}(\xi, \eta) \mathbf{P}_{i,j}. \quad (6)$$

If $w_{i,j}$ is the same value for all i and j , then $\mathbf{S}(\xi, \eta)$ becomes a rational B-spline surface. Much of the utility of both surface modeling and IGA is owed to the advantageous characteristics of these functions; more of the mathematical details of NURBS are given by Piegl and Tiller³⁴ and Hughes et al.¹⁸ IGA relies on the utilization of such functions to derive appropriate variational formulations for partial differential equations. In other words, in, for example, NURBS-based IGA, the governing equations are discretized directly using NURBS. For structural IGA, the degrees of freedom are usually the displacements of the control points.

A cursory comparison of NURBS basis functions and Lagrange basis functions is shown in Figure 1. In both cases, quadratic basis functions are used to span three elements. As is the case in traditional FEA, the concept of "elements" is employed in IGA. In NURBS-based IGA, the spaces in between the knots in a valid knot vector are considered elements. For example, given the knot vector of $\Xi = [0, 0, 0, 1, 2, 3, 3, 3]$, the parametric space $\xi = [0, 1]$ is considered an element. This definition is employed despite the fact that some of basis functions that are active in the space of this element remain active beyond $\xi = 1$, a key distinction from traditional finite elements. Also as in traditional FEA, mesh refinement is an important procedure in IGA. Both h -refinement, which corresponds to *knot insertion* of NURBS functions, and p -refinement, which corresponds to *degree elevation*, are possible. p -refinement entails changing the degree of the functions being used (e.g. NURBS), whereas h -refinement inserts knots to "divide" elements. k -refinement, which consists of p -refinement followed by h -refinement, is also possible in IGA and has some beneficial qualities. For more information, details about both IGA and the use of NURBS in the context of IGA are described by Hughes et al.¹⁸

Some efficiency comparisons of IGA and traditional FEA have been performed in the literature. For example, Benson et al.¹⁹ demonstrated that structural analysis of a roof using 4,512 linear Belytschko–Tsay elements produced accurate results in 10.5 CPU seconds. Alternatively, using IGA, results of equivalent accuracy were obtained in 2.90 CPU seconds using only 450 quadratic NURBS elements. Such performance improvements can be observed in other contexts as well, especially when complex geometries are involved.^{20,35} This underscores the efficient nature of IGA.

2.2 | Isogeometric analysis of thin-shell composites

Wind turbine blades are commonly analyzed as shell structures. An isogeometric Kirchhoff–Love thin-shell formulation was first proposed by Kiendl et al.³⁶ and was reformulated for composite shells by Bazilevs et al.²² The thin-shell formulation was shown by Korobenko et al.²⁶ to accurately model wind turbine blade kinematics. Furthermore, the thin-shell formulation is computationally advantageous relative to thick-shell formulations in that it does not feature rotational degrees of freedom. This makes it a particularly appropriate formulation for the purposes of iterative design.

In Kirchhoff–Love shell theory, the Green–Lagrange strain tensor, \mathbf{E} , can be expressed as a combination of the membrane strain tensor, $\boldsymbol{\varepsilon}$, and curvature change tensor, $\boldsymbol{\kappa}$, at the shell midsurface:

$$\mathbf{E} = \boldsymbol{\varepsilon} + \zeta \boldsymbol{\kappa}, \quad (7)$$

where ζ is the through-thickness coordinate. For the problems considered in this work, a linear stress–strain relationship is assumed:

$$\mathbf{S} = \mathbf{C} \mathbf{E}, \quad (8)$$

where \mathbf{S} is a second Piola–Kirchhoff stress tensor and \mathbf{C} is a constitutive material tensor. Integrating the stress through the thickness, one can define the stress resultant due to membrane action, \mathbf{N} , and the stress resultant due to bending action, \mathbf{M} . Where composites are used, these may be defined as

$$\mathbf{N} = \mathbf{A} \boldsymbol{\varepsilon} + \mathbf{B} \boldsymbol{\kappa}, \quad (9)$$

$$\mathbf{M} = \mathbf{B} \boldsymbol{\varepsilon} + \mathbf{D} \boldsymbol{\kappa}. \quad (10)$$

\mathbf{A} , \mathbf{B} , and \mathbf{D} are the extensional (membrane), coupling, and bending stiffness tensors, respectively, calculated using classical laminated plate theory.³⁷ In this work, these tensors are written with respect to the local Cartesian basis; the local Cartesian basis is oriented on the first covariant base vector of the midsurface, which is aligned with the first parametric direction of the NURBS surface. Employing the concept of virtual work, the final structural formulation may be obtained as

$$\delta W^{\text{int}} - \delta W^{\text{ext}} = 0, \quad (11)$$

where

$$\delta W^{\text{int}} = \int_S \int_{\zeta} \delta \mathbf{E} : \mathbf{S} \, d\zeta \, dS = \int_S (\delta \boldsymbol{\varepsilon} : \mathbf{N} + \delta \boldsymbol{\kappa} : \mathbf{M}) \, dS = \int_S \delta \boldsymbol{\varepsilon} : (\mathbf{A} \boldsymbol{\varepsilon} + \mathbf{B} \boldsymbol{\kappa}) \, dS + \int_S \delta \boldsymbol{\kappa} : (\mathbf{B} \boldsymbol{\varepsilon} + \mathbf{D} \boldsymbol{\kappa}) \, dS, \quad (12)$$

and

$$\delta W^{\text{ext}} = \int_S \delta \mathbf{u} \cdot \mathbf{f} \, dS. \quad (13)$$

In the above, S denotes the shell midsurface in the reference configuration. $\delta \boldsymbol{\varepsilon}$ and $\delta \boldsymbol{\kappa}$ are the virtual counterparts of $\boldsymbol{\varepsilon}$ and $\boldsymbol{\kappa}$, respectively, corresponding to a virtual displacement vector $\delta \mathbf{u}$. The load vector \mathbf{f} represents both distributed external loads as well as (thickness-integrated) body loads.

In the context of IGA, Equation 11 is discretized using, for example, NURBS, as Kiendl³⁸ describes in detail. Because second order derivatives appear in the governing variational equations of the Kirchhoff–Love theory, C^1 -continuous approximation functions are required. This implies that traditional low-order finite element approaches cannot be readily used to perform thin-shell analysis. In contrast, CAD-based functions, such as NURBS, are naturally C^1 -continuous and can be directly employed for thin-shell analysis.

2.3 | Coupling of surface patches with matching or non-matching discretization

Despite the many advantages offered by the isogeometric Kirchhoff–Love approach, maintaining C^1 continuity of the approximation functions throughout the entirety of a given structure is often unfeasible. Real-world objects are commonly composed of many NURBS surface patches. This can be a result of the underlying CAD technology, designer intent, or some combination thereof. Models composed of multiple patches have C^0 or even C^{-1} continuity between patches, the latter meaning that small gaps or overlaps between adjacent patches might appear. Such situations naturally occur in the modeling of wind turbine blades because the outer shell of the blade and its shear webs cannot be modeled using a single NURBS patch.

A variety of approaches for coupling thin-shell components have been offered in the field of IGA.^{39–45} One of the most well-known methods is the bending strip method, first introduced by Kiendl et al.⁴⁶ The method introduces NURBS-based strips of fictitious material featuring unidirectional bending stiffness and zero membrane stiffness. In multiple instances,^{22,27,46} bending strips were shown to be effective for performing IGA-based simulation of multi-patch wind turbine blade structures. A key drawback of the bending strip method, however, is that it requires the NURBS control points on two coupled patches to be coincident at the coupling location. This arrangement is also known as conforming discretization. Conforming

discretization is difficult to achieve in many circumstances, wind turbine blade modeling included, and requiring it greatly constrains the geometry construction procedure.

A coupling approach that is capable of coupling patches with non-matching interfaces was proposed by Breitenberger et al.⁴³ In that work, both displacement and rotational continuity are imposed via penalty formulations. However, the formulation for rotational continuity was restricted to rotation angles less than $\pi/2$. Duong et al.⁴⁵ presented a different penalty formulation for rotational continuity which has no limitation on the rotational angle but which is only applied to conforming patches. In the present paper, the approach presented by Duong et al.⁴⁵ is extended to non-matching patches in order to maximize the flexibility of the coupling methodology.

Consider a patch interface between two surface patches S^A and S^B . These patches might be used to model, for example, a wind turbine blade's shear web and spar cap as shown in Figure 2. Note that the two patches do not have conforming discretization. In order to avoid undesirable jumps in displacements and rotations at the patch interfaces, two separate penalty energies are defined. The displacement penalty virtual work is obtained in a standard form as

$$\delta W^{pd} = \int_{\mathcal{L}^{AB}} \alpha_d (\delta \mathbf{u}^A - \delta \mathbf{u}^B) \cdot (\mathbf{u}^A - \mathbf{u}^B) d\mathcal{L}. \quad (14)$$

\mathcal{L}^{AB} denotes the patch interface, \mathbf{u}^A and \mathbf{u}^B are the displacements of the corresponding points on surface patches S^A and S^B , respectively, and α_d is a penalty parameter of large magnitude. For the rotational continuity between the two surfaces, the rotational penalty virtual work⁴⁵ is defined

$$\delta W^{pr} = \int_{\mathcal{L}^{AB}} \alpha_r ((\delta \cos \phi - \delta \cos \phi_0) (\cos \phi - \cos \phi_0) + (\delta \sin \phi - \delta \sin \phi_0) (\sin \phi - \sin \phi_0)) d\mathcal{L}, \quad (15)$$

where ϕ_0 and ϕ are the angles between the surfaces before and after deformation, respectively. The virtual work formulation, Equation 11, is augmented by δW^{pd} and δW^{pr} and restated as

$$\delta W^{int} + \delta W^{pd} + \delta W^{pr} - \delta W^{ext} = 0. \quad (16)$$

For more details on the variations of the penalty energies, the reader is referred to Duong et al.⁴⁵

An inherent issue in penalty methods is the choice of penalty parameters. If the value of the penalty parameter is too low, the constraint is not satisfied accurately enough. If the penalty parameter value is too high, the matrices may become ill-conditioned and the solution of the linear system is prone to large numerical errors. Ideally, penalty formulations should scale with geometric and material properties of the problem at hand in a way that makes the choice of the penalty parameters problem-independent. In the present framework the two penalty parameters α_d and α_r are linked to a single dimensionless parameter, α , as follows:

$$\alpha_d = \alpha \frac{\min(\max_{i,j}(A_{ij}^A), \max_{i,j}(A_{ij}^B))}{(h^A + h^B)/2} \quad i = 1, 2, \quad j = 1, 2, \quad (17)$$

$$\alpha_r = \alpha \frac{\min(\max_{i,j}(D_{ij}^A), \max_{i,j}(D_{ij}^B))}{(h^A + h^B)/2} \quad i = 1, 2, \quad j = 1, 2. \quad (18)$$

A_{ij}^A and A_{ij}^B are the elements of local extensional stiffness matrices on surfaces S^A and S^B determined using classical laminated plate theory,³⁷ D_{ij}^A and D_{ij}^B are the elements of local bending stiffness matrices, and h^A and h^B are the length of the local elements in the direction most parallel to the penalty curve \mathcal{L}^{AB} . This formulation, along with an overall penalty parameter of $\alpha = 10^3$, works effectively for a wide range of blade analyses, reducing the extent to which the penalty-based approach is problem-dependent.

The interface curve \mathcal{L}^{AB} is a NURBS curve that can be easily generated for arbitrary configurations in most CAD systems. When performing numerical integration of Equations 14 and 15, the integrands must be evaluated at quadrature points along \mathcal{L}^{AB} which requires information from both surfaces S^A and S^B . For configurations in which a mapping between the parametric spaces of \mathcal{L}^{AB} , S^A , and S^B can be easily determined, this evaluation is straightforward. For more complex configurations, especially when \mathcal{L}^{AB} is an approximation of the intersection of surfaces S^A and S^B , this information is obtained from the points on S^A and S^B nearest to a given quadrature point on \mathcal{L}^{AB} .

2.4 | Parametric generation of blade geometry

Reliable, parametric generation of IGA-suitable NURBS geometries is a nontrivial task. NURBS-based CAD geometries commonly contain small gaps, overlaps, and trimmed NURBS regions. In IGA, such issues must be carefully avoided or mitigated because the functions are directly employed for discretization purposes. Thus, given a wind turbine blade's design parameters, it is critical to employ a set of geometric operations that will generate a model to which Equation 16 can be applied. Additionally, for the purposes of design, this set of operations should be applicable across a range of design parameters. Following the work presented by Herrema et al.,³¹ the CAD software Rhinoceros 3D, a purely NURBS-based platform, and Grasshopper 3D, a visual programming interface for Rhinoceros, are employed. The programmatic approach of Grasshopper allows consistent

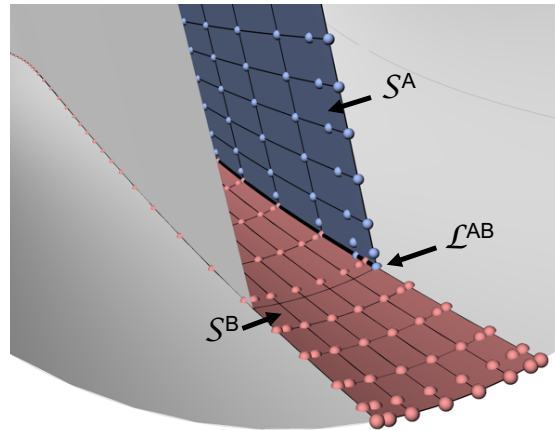


FIGURE 2 Two NURBS surfaces, S^A and S^B , representing the shear web and spar cap of a wind turbine blade. The surfaces must be coupled along the curve L^{AB} . Control point locations are indicated by spheres.

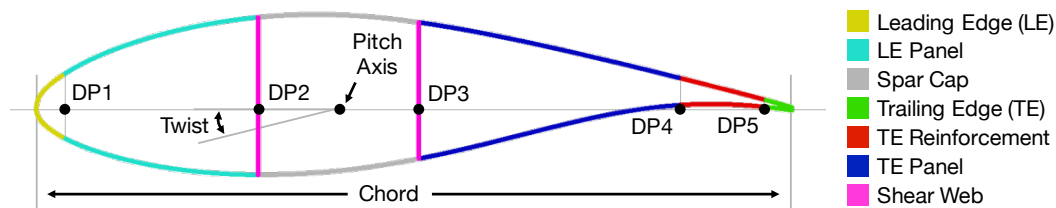


FIGURE 3 Illustration of parameters defined at each station along the blade span in order to define blade geometry and material regions. Parameter values for the NREL/SNL 5 MW blade are given in Table A1.

generation of geometries for a range of parametric inputs whereas its interactive nature enables efficient, intuitive alteration of the underlying algorithms used to generate geometries. The algorithm used to generate the wind turbine blade geometry featured in this work is fundamentally the same as that presented by Herrema et al.³¹ However, the algorithm has been enhanced to facilitate flatback airfoils, generation of shear web geometries, and division of the high- and low-pressure surfaces into distinct material zones. While a single geometry is used in this work, this approach could be used to generate a wide range of blade geometries.

3 | 5 MW BLADE ANALYSIS

In order to demonstrate the effectiveness of the framework described in Section 2, the NREL/SNL 5 MW reference blade is modeled and analyzed. After defining the reference 5 MW wind turbine blade model in Section 3.1, the model is verified with respect to the reference⁴⁷ in Section 3.2. Mass, vibration, and buckling analyses are used and mesh refinement studies are performed throughout. The studies underscore the attractive performance of the IGA-based framework.

3.1 | NREL/SNL 5 MW blade model

The National Renewable Energy Laboratory (NREL) 5 MW blade was first introduced by Jonkman et al.⁴⁸ in the context of a full 5 MW turbine definition which was intended to be a reference for offshore system development. The turbine is a three-bladed, upwind, variable-speed, variable-pitch machine that is loosely representative of modern utility-scale turbines. The geometric definition of the NREL 5 MW blade itself, however, was only intended to support basic aerodynamic analysis and did not contain enough detail to support construction of a three-dimensional CAD model. Furthermore, only the distributed structural properties of the blade are given, rather than a complete composite layup. Resor,⁴⁷ as a part of Sandia National Laboratories (SNL), therefore established a rudimentary structural design that approximately reproduces the distributed structural

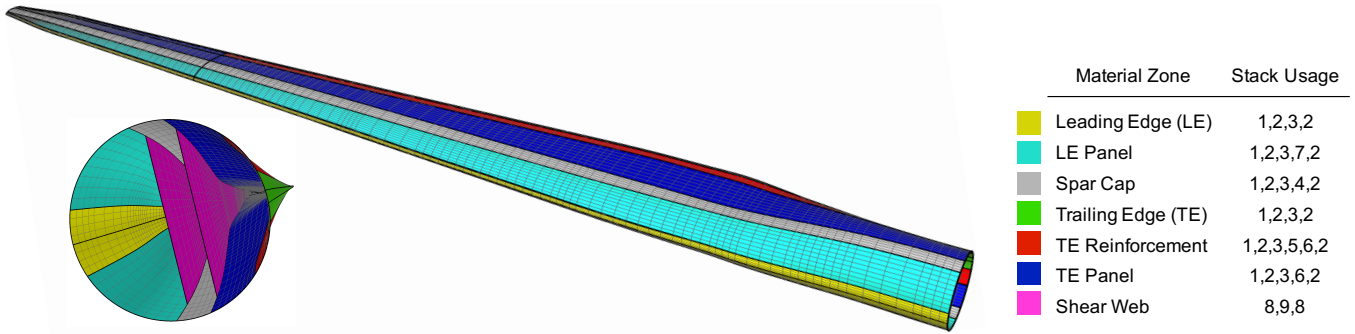


FIGURE 4 A NURBS-based model of the NREL/SNL 5 MW blade. Colors indicate zones with distinct material stacking sequences. Grey lines indicate element edges and black lines indicate surface patch edges. Stacking sequence for each material zone provided; stack definitions can be found in Figure 5.

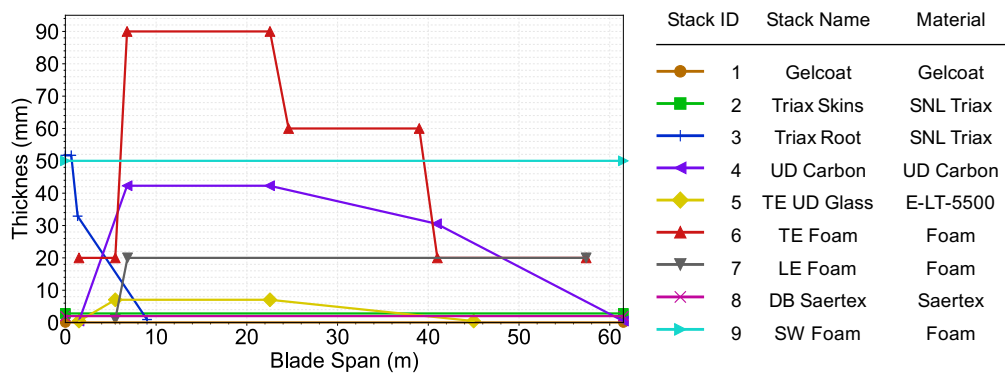


FIGURE 5 Definition of material stack spanwise thickness distributions and properties.⁴⁷

properties described by Jonkman et al.⁴⁸ The design also includes a more detailed geometry definition that is suitable for generation of high quality surface geometries. The wind turbine blade definition described in Resor et al.⁴⁷ will hereafter be referred to as the NREL/SNL 5 MW blade.

The properties of each airfoil cross section describing the NREL/SNL 5 MW blade are given in Table A1. The table defines the properties needed to establish a baseline aerodynamic profile, including airfoil type, twist degree, and pitch axis location. It also describes the location of the material division points needed to divide the blade into distinct material zones. The parameters that are defined at each spanwise station are illustrated in Figure 3.

Along with the geometry generation approach described in Section 2.4, the parameter values given in Table A1 are used to develop a NURBS-based shell model, shown in Figure 4. The model consists of 21 NURBS surfaces, of degree 3 in both parametric directions, and 51 penalty coupling curves. Each NURBS surface is assigned to a material zone with a distinct material stacking sequence, indicated by color in Figure 4. The relatively high spanwise resolution of cross sections in Table A1 is not actually required to maintain geometric accuracy. However, the modeling software used by Resor⁴⁷ assumes that stacks of materials have constant thickness between stations. This requires that many interpolated stations must be defined to sufficiently represent significant ply drops. In the present work, material thicknesses are defined as piecewise linear functions of blade span which are evaluated at every integration point to determine material distribution. This simplification eliminates the need to use all stations for model construction. More information is given in the footnotes of Table A1.

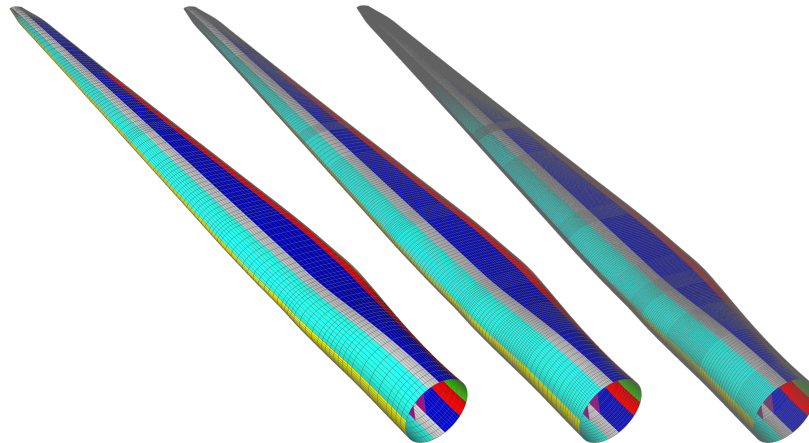
Each of the material zones indicated in Figure 4 employs a unique sequence of material stacks. Each of these material stacks consists of a single orthotropic material with a distinct spanwise thickness distribution as defined in Figure 5. Material properties are described in Table 1 where E_1 and E_2 are the Young's moduli in the first and second material directions, respectively; G_{12} is the shear modulus; ν_{12} is Poisson's ratio; ρ is the density; σ_{UT} is the ultimate tensile strength; and σ_{UC} is the ultimate compressive strength. Further details are given by Resor⁴⁷ and Griffith and Ashwill.⁴⁹ As Griffith and Ashwill explain, the material properties reported in Table 1 for Saertex and SNL Triax represent the homogenized properties of layups having non-uniform, symmetric fiber orientations. Thus, in the stacking sequences described in Figure 4, these homogenized materials, and all other materials, are assumed to have an overall fiber orientation of zero degrees. In this work, the material axes are aligned with the local Cartesian basis. As a result, the first material direction is aligned with the spanwise parametric direction of the local NURBS surface patch.

TABLE 1 Orthotropic material properties used in the NREL/SNL 5 MW blade design.

Material Name	Layer Thickness (mm)	E_1 (GPa)	E_2 (GPa)	G_{12} (GPa)	ν_{12} (-)	ρ (kg/m ³)	σ_{UT} (GPa)	σ_{UC} (GPa)
Gelcoat	0.05	3.440	3.440	1.323	0.30	1235	-	-
E-LT-5500	0.47	41.80	14.00	2.630	0.28	1920	0.972	0.702
SNL Triax	0.94	27.70	13.65	7.200	0.39	1850	0.700	-
Saertex	1.00	13.60	13.30	11.80	0.49	1780	0.144	0.213
Foam	1.00	0.256	0.256	0.022	0.30	200	-	-
UD Carbon	0.47	114.5	8.390	5.990	0.27	1220	1.546	1.047

TABLE 2 Blade mass property comparisons for the reference and presented models.

Property	Ref ⁴⁷	Mesh 1	Mesh 2	Mesh 3
Mass (kg)	17 700	17 184	17 183	17 183
Center of Mass (m)	19.102	19.373	19.373	19.373
First Mass Moment of Inertia (kg-m)	3.381×10^5	3.329×10^5	3.329×10^5	3.329×10^5
Second Mass Moment of Inertia (kg-m ²)	1.100×10^7	1.079×10^7	1.079×10^7	1.079×10^7

**FIGURE 6** IGA Mesh 1, Mesh 2, and Mesh 3 (left to right).

3.2 | Model verification

3.2.1 | Mass properties

The fundamental mass properties of NURBS-based models with three levels of discretization are compared with the reference⁴⁷ 5 MW blade model. Mesh 1, shown in Figure 4, consists of 10 800 cubic NURBS elements and 16 367 control points over the 28 NURBS surfaces. Mesh 2 is obtained by performing a single global h-refinement of Mesh 1, and Mesh 3 is obtained by performing two global h-refinements of Mesh 1. These meshes are shown in Figure 6. As discussed previously, the presented model and the reference model use different approaches for modeling material thickness distributions. Additionally, it is likely that slight geometrical differences exist, and it appears that Resor⁴⁷ employs a level of discretization that does not yet produce converged solutions. Some differences in model properties are therefore expected. In general, however, as Table 2 demonstrates, the fundamental blade mass properties compare favorably. The NURBS-based model is somewhat lighter overall with a center of mass slightly outboard compared with the reference blade. All three models have exactly the same area, 603.0 m², because, when h refinement is used in IGA, the geometry remains unchanged. The mass differs slightly for Mesh 1, however, because the linear thickness distributions are being approximated with discretization-dependent continuous functions. In general all of the listed properties are nearly identical for all three levels of NURBS discretization.

TABLE 3 Frequencies of vibration of the reference model and the IGA-based model with three levels of discretization. Blade modes depicted in Figure 7.

	Ref ⁴⁷	Mesh 1		Mesh 2		Mesh 3	
		Freq (Hz)	Diff (%)	Freq (Hz)	Diff (%)	Freq (Hz)	Diff (%)
1st flapwise ^a	0.87	0.919	5.63	0.919	5.63	0.919	5.63
1st edgewise ^b	1.06	1.054	0.57	1.054	0.57	1.053	0.66
2nd flapwise ^c	2.68	2.809	4.81	2.808	4.78	2.808	4.78
2nd edgewise ^d	3.91	3.886	0.61	3.884	0.66	3.883	0.69
3rd flapwise ^e	5.57	5.666	1.72	5.660	1.62	5.658	1.58
1st torsion ^f	6.45	6.698	3.84	6.694	3.78	6.692	3.75

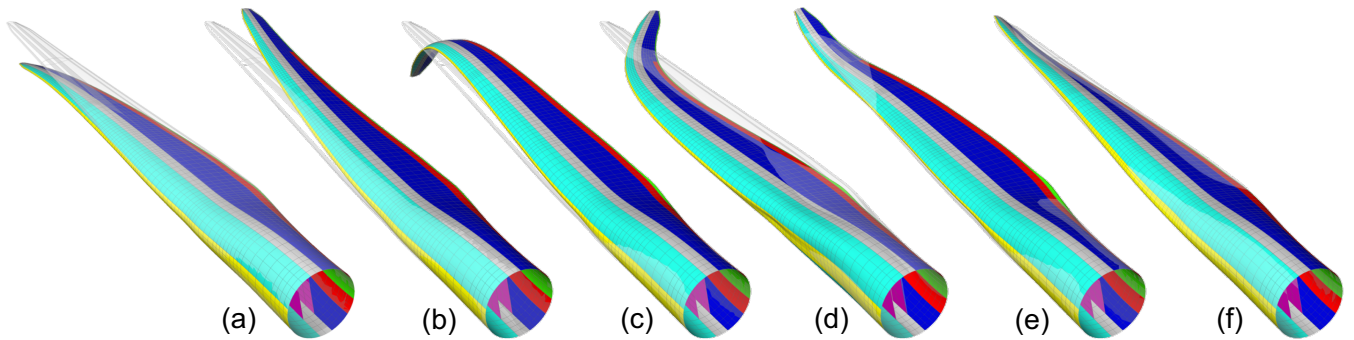


FIGURE 7 The first six vibration modes, described in Table 3, for Mesh 1 of the IGA-based blade model.

3.2.2 | Vibration analysis

Having constructed a model of the NREL/SNL 5 MW blade that is suitable for IGA, a variety of analyses can be performed using the methodology described in Section 2. The vibrational frequencies of a wind turbine blade are important to quantify throughout design in order to avoid resonance phenomena. Because vibration analysis incorporates both the mass properties and the stiffness properties of a structure, it is also a good candidate for comparing the presented IGA-based 5 MW model to the reference model. In the finite element context, linear vibration analysis can be performed by considering the eigenvalue problem

$$\left(\mathbf{K}^{\text{lin}} - \lambda_i \mathbf{M}\right) \mathbf{v}_i = 0, \quad (19)$$

where \mathbf{K}^{lin} is the linear stiffness matrix of the structure, \mathbf{M} is the mass matrix, and λ_i is the i^{th} eigenvalue associated with mode vector \mathbf{v}_i . The relation of the i^{th} frequency of vibration, ω_i , to the eigenvalue is given by the equation $\omega_i^2 = \lambda_i$. The eigenvalue problem in Equation 19 is solved within the scientific software package SLEPc,^{50,51} which is based on the software package PETSc.^{52,53} Specifically, the SLEPc-default Krylov-Schur solver is used with a shift-and-invert spectral transformation for extraction of interior eigenvalues.

The calculated frequencies of both the reference and the IGA-based model are reported in Table 3, with three levels of discretization used for the IGA-based model. The blade modes, \mathbf{v}_i , of Mesh 1 are depicted in Figure 7. As discussed previously, some variation in computed frequencies of vibration is expected due to a few differences in modeling strategies. As Table 3 shows, however, the first six computed frequencies all agree reasonably well, with a largest difference of 5.63%, or approximately 0.05 Hz, and a lowest difference of 0.61%.

3.2.3 | Buckling analysis

As discussed in Section 1, buckling load factor calculation is one of the key applications of high-fidelity structural analysis methods in blade design. Linear buckling analysis, or eigenvalue buckling analysis, entails solving the equation

$$\left(\mathbf{K}^{\text{lin}} + \lambda_i \mathbf{K}_g\right) \mathbf{v}_i = 0. \quad (20)$$

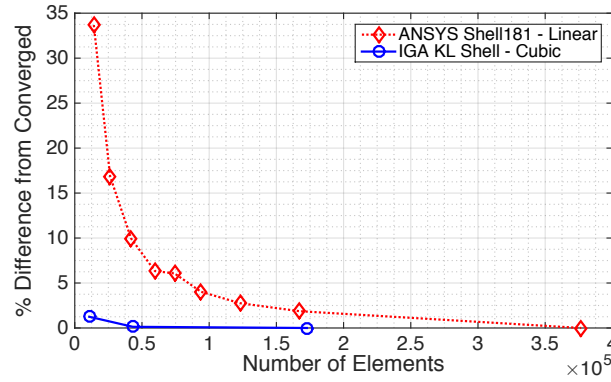


FIGURE 8 Convergence of lowest predicted buckling load factor relative to the most converged solution under mesh refinement for both IGA computations (blue) and computations performed by Resor⁴⁷ (red).

\mathbf{K}^{lin} is the linear stiffness matrix of the structure, \mathbf{K}_g is the geometric stiffness matrix⁵⁴ calculated based on critical aerodynamic load conditions, and λ_i is the i^{th} eigenvalue associated with mode vector \mathbf{v}_i . In this context, an eigenvalue λ_i is a scalar multiplier of the applied loads that will, in theory, cause buckling of the structure. The PETSc-based SuperLU_DIST⁵⁵ direct solver is employed to solve the initial linear problem posed by Equation 16 prior to constructing \mathbf{K}_g . The eigenvalue problem posed in Equation 20 is addressed by again employing the SLEPc-based Krylov–Schur solver with a shift-and-invert spectral transformation.^{50,51}

Comparison of IGA buckling results to the reference results is complicated by the fact that buckling analysis is load-dependent. Load distributions are not provided by Resor⁴⁷; hence, aeroelastic simulations, from which distributed loads can be extracted, are performed. This process will be described in greater detail in Section 4.1. For the purposes of simple comparison, the extreme 50-year wind load case with 15 degrees of yaw error is simulated and the instantaneous aerodynamic loads corresponding to the maximum flapwise root bending moment are applied. In the presented framework, these loads are distributed to all blade surfaces evenly in the chordwise direction and varying in the spanwise direction according to the load profile produced by aeroelastic analysis. The force yielded by aeroelastic analysis is converted to a traction which is applied to the NURBS surfaces.

Within the IGA-based framework, a buckling factor of 1.61 is calculated. This factor is within 2% of the lowest buckling factor of 1.64 reported by Resor for the same load case.⁴⁷ Additionally, the mode shape, which shows buckling focused in the spar cap, is very similar to some of the mode shapes shown by Resor.⁴⁷ However, this mode occurs at a different load factor in the work of Resor.⁴⁷ This difference is likely due, in part, to differences in the aerodynamic load distributions.

3.2.4 | Mesh refinement study

Mesh refinement studies using mass and vibration analyses were performed in previous sections. However, Resor⁴⁷ performs a mesh refinement study via linear buckling analysis. Thus, in this section, a similar, IGA-based mesh refinement study is performed for comparison.

Resor⁴⁷ performs a mesh refinement study for flapwise buckling of the NREL/SNL 5 MW blade modeled in ANSYS,⁵⁶ the results of which are reproduced in Figure 8. Resor⁴⁷ applies a load distribution intended to recreate the maximum bending moment distribution experienced along the blade span. For the IGA-based study, a simplified approach in which the loads corresponding to largest flapwise root bending moment, described in Section 3.2.3, are employed. Resor⁴⁷ performs mesh refinement by incrementally reducing the target element size used in a meshing algorithm, whereas refinement in the IGA framework is performed via h-refinement, described previously.

Figure 8 shows the results of the two mesh refinement studies. The resultant buckling loads are normalized with respect to the most refined solution. It should be noted that the results in Figure 8 do not constitute a one-to-one comparison of traditional FEA to IGA. The element employed by Resor,⁴⁷ ANSYS Shell181, is a four-node, thick-shell, linear element with six degrees of freedom at each node. The IGA model employs a thin-shell formulation and cubic NURBS with three degrees of freedom at each node. The total number of degrees of freedom (DOF) used in an analysis is significant because it indicates the size of the linear algebra problem that must be solved; smaller problems can typically be solved more quickly. Resor⁴⁷ only provides the number of elements used in the reference analysis, and the number of elements and DOF cannot be directly related without any knowledge of the mesh topology. Still, the relative number of elements is at least indicative of the relative number of DOF, and hence the linear algebra problem size, especially for meshes with fairly uniform discretization.

The results in Figure 8 demonstrate the efficiency of the presented IGA approach relative to a more traditional FEA approach. For the coarsest ANSYS-based case having approximately 14 200 elements, an error of approximately 34% is observed. In sharp contrast, when using 10 800

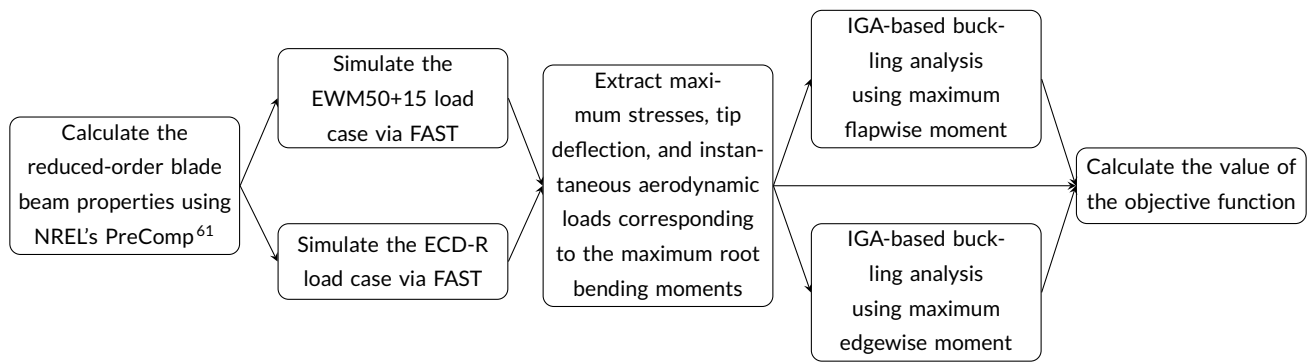


FIGURE 9 Function evaluation procedure for a given set of design variables.

elements in the IGA framework an error of only 1.25% is observed, a level of error that is not achieved even by using more than 160 000 ANSYS Shell181 elements. Additionally, moderate refinement quickly drives error towards zero for isogeometric analysis.

4 | DESIGN OPTIMIZATION

The efficiency of the IGA-based framework for wind turbine blade analysis underscores its value in the context of iterative analysis. Not only can the use of IGA provide time savings but it can also provide benefits in regards to other practical issues such as mesh generation, data transfer, and data storage. Thus, this section utilizes the aforementioned framework to perform IGA-buckling-constrained optimization of the blade mass and material cost of the NREL/SNL 5 MW blade.

Here, optimization is the primary design approach. A designer may employ other design strategies, such as manual iterations, sensitivity studies, etc. One may also employ different optimization methods than the methods employed in this work. It is likely that other design strategies would lead to different results than those presented here. However, the IGA-based framework for wind turbine blade analysis could still be beneficially employed within any of these other strategies.

4.1 | Aeroelastic simulation

A critical task in wind turbine blade design is quantification of the aerodynamic loads, a complicated endeavor due to the interdependence of aerodynamic and structural factors. Advanced aeroelastic codes such as FAST⁵⁷ and HAWC2⁵⁸ utilize reduced-order models to predict overall wind turbine behavior subject to the effects of aerodynamics, structural dynamics, control, and other factors. For the present optimization problem, NREL's FAST is employed in conjunction with high-fidelity IGA. Load analysis is performed using the methodology presented by Resor.⁴⁷ Resor⁴⁷ identifies a subset of IEC 61400 design load cases (DLCs) that are considered to be the most likely design drivers for a 5 MW wind turbine blade: DLCs 1.2, 1.3, 1.4, 1.5, 1.6, and 6.3.

For the purposes of comparison, the evaluation of these load cases, as outlined by Resor,⁴⁷ is reproduced using FAST version 8. FAST is implemented in the style of the Framework for Unified Systems Engineering and Design of Wind Plants (FUSED-Wind),⁵⁹ an open-source framework for multidisciplinary optimization of wind energy systems which was developed as an extension to the NASA-developed OpenMDAO.⁶⁰ While the exact results obtained differ somewhat from those reported by Resor⁴⁷ because of slightly different material distributions, different versions of FAST, and potentially different simulation settings that are not described by Resor⁴⁷, the overall trends and conclusions corroborate the reference analysis. Neither ultimate stress analysis nor fatigue analysis are shown to be design-governing, with all stress values falling below the design limits for each material and Miner's fatigue analysis indicating a material life of well over 20 years. A maximum tip deflection of 6.34 m is observed during the load case featuring a negative gust at rated speed (ECD-R), whereas a maximum flapwise moment of 23 130 kN is observed during the 50-year extreme wind load case with positive 15 degrees of yaw misalignment (EWM50+15). The aerodynamic loads corresponding to this case are used to calculate the buckling load factor of 1.61 discussed in Section 3.2.3.

Given that the NREL/SNL 5 MW reference blade design appears to be governed by the EWM50+15 and ECD-R load cases, only these cases are utilized in the demonstration optimization problem. In reality, the governing load cases may change as the design evolves; this fact must be carefully considered in the industrial design context. For each set of design parameters, the procedure for determining objective function value is summarized in Figure 9.

TABLE 4 The price of the various materials used in the NREL/SNL 5 MW blade design. Fiberglass costs (E-LT-5500, SNL Triax, and Saertex) are based on dry fiber material whereas UD Carbon material is pre-impregnated.

Material	Price (\$/kg)	Kitting Cost (\$/m ²)	Thickness Cost (\$/mm)
Foam	-	20.00	0.50
Gelcoat	14.00	-	-
E-LT-5500	2.97	-	-
SNL Triax	2.97	-	-
Saertex	2.97	-	-
Resin	4.65	-	-
UD Carbon	26.40	-	-

4.2 | Objective function

The ultimate goal throughout the design of any wind turbine component is to reduce the overall cost of energy. Two primary ways to achieve this are reduction of total blade material cost and reduction of blade mass. Blade mass reduction entails reduced loads on the nacelle and tower, which could lead to reduced cost overall. Blade material cost is more obviously a contributor to turbine capital cost.

The optimization problem is therefore posed as follows:

$$\begin{aligned}
 & \text{minimize} && f(\mathbf{x}) \\
 & \text{subject to} && c_i(\mathbf{x}) \leq 0, \quad i = 1, \dots, n_c, \\
 & && \mathbf{x} \in \Omega.
 \end{aligned} \tag{21}$$

\mathbf{x} are the design variables, $f(\mathbf{x})$ is the objective function, $c_i(\mathbf{x})$ are the n_c inequality constraints, and Ω are the acceptable ranges for the design variables. The objective function is defined

$$f(\mathbf{x}) = w \frac{M(\mathbf{x}) - M_{\text{ref}}}{M_{\text{ref}}} + (1 - w) \frac{C(\mathbf{x}) - C_{\text{ref}}}{C_{\text{ref}}}, \tag{22}$$

where $M(\mathbf{x})$ is the blade mass for a given set of design variables, M_{ref} is the mass of the reference blade design, $C(\mathbf{x})$ is the total blade material cost for a given set of design variables, C_{ref} is the reference total material cost, and w is the weighting variable indicating the relative importance of mass and cost reduction, respectively. Market factors, blade transportation, systems-level interactions, and numerous other factors can influence the optimal weighting for a given design scenario. It is not within the scope of this work to incorporate such factors; thus, a weighting of $w = 0.5$ is used for demonstration purposes. Blade mass is calculated using the various material densities given by Resor.⁴⁷ The cost of the majority of the materials is dictated by the price per kilogram reported by Griffith and Johanns,⁶² summarized in Table 4. Fiberglass materials are priced as dry fibers; the fiber volume fractions and the cost of resin can be used to determine the infused cost. Alternatively, foam core is priced first on the basis of kitted area and then according to material thickness.

4.3 | Constraints

One can restate the constrained optimization problem, Equation 21, as an unconstrained optimization problem by incorporating the constraints into the original objective function using the exterior penalty method.⁶³ This yields a pseudo-objective function

$$\Phi(\mathbf{x}) = w \frac{M(\mathbf{x}) - M_{\text{ref}}}{M_{\text{ref}}} + (1 - w) \frac{C(\mathbf{x}) - C_{\text{ref}}}{C_{\text{ref}}} + \sum_{i=1}^{n_c} \beta_i \max(0, c_i(\mathbf{x}))^2, \tag{23}$$

where β_i is a large penalty parameter. An unconstrained optimization problem is ultimately solved:

$$\begin{aligned}
 & \text{minimize} && \Phi(\mathbf{x}) \\
 & \text{subject to} && \mathbf{x} \in \Omega.
 \end{aligned} \tag{24}$$

This exterior penalty strategy presents a straightforward but effective way to incorporate constraints into the objective function. The strategy is also beneficial in that it greatly increases the number of optimization methods that can be used to solve the problem.

Upon simulating the EWM50+15 and ECD-R load cases in FAST, many of the constraints $c_i(\mathbf{x})$ can be directly calculated. One set of constraints is used to state that the maximum stresses in each structural material across the entirety of the blade should not exceed the material's maximum

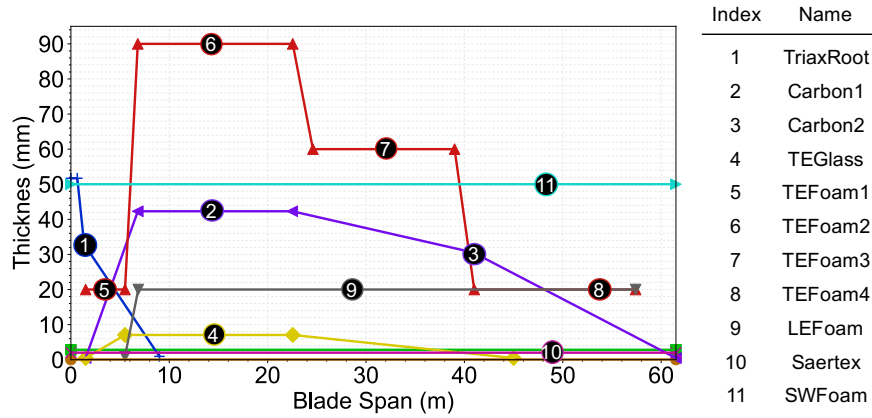


FIGURE 10 Material stack thickness distributions with design variables identified by numerical markers. Indices of the variables Δt_i and corresponding names given at right.

tensile strength with respect to a load factor:

$$c_j(\mathbf{x}) = \sigma_{\max_j}(\mathbf{x}) - \frac{\sigma_{UT_j}}{\gamma_u} \leq 0, \quad j = 1, \dots, n_m. \quad (25)$$

σ_{\max_j} is the maximum stress experienced by each material, σ_{UT_j} is the ultimate tensile strength of the material, n_m is the number of materials for which failure is a design concern, and γ_u is the safety factor used for evaluation of ultimate strength. For this work, $\gamma_u = 1.755$.⁴⁷ Stresses are calculated using the approach described by Resor.⁴⁷

A tower clearance constraint can be similarly defined:

$$c_{n_m+1}(\mathbf{x}) = \delta_{\text{tip}}(\mathbf{x}) - \frac{\delta_{\text{avail}}}{\gamma_t} \leq 0, \quad (26)$$

where δ_{tip} is the maximum out-of-plane displacement experienced by any of the blades throughout all simulations, δ_{avail} is the available tower clearance, and γ_t is the safety factor used for tip clearance evaluation. Here, $\delta_{\text{avail}} = 10.50$ m and $\gamma_t = 1.485$.⁴⁷

Lastly, after extracting the aerodynamic loads that produce the maximum bending moment in both the flapwise and edgewise directions, IGA-based linear buckling analysis can be performed. The corresponding constraint is given as

$$c_{n_m+2}(\mathbf{x}) = \gamma_b - \min(\lambda_{\text{flap}}(\mathbf{x}), \lambda_{\text{edge}}(\mathbf{x})) \leq 0, \quad (27)$$

where λ_{flap} is the lowest buckling load factor as a result of the loads corresponding to the maximum flapwise bending moment, λ_{edge} is the lowest buckling load factor as a result of the loads corresponding to the maximum edgewise bending moment, and γ_b is the factor of safety used for linear buckling evaluation; in this case, $\gamma_b = 1.62$. All design load factors are the same as those used by Resor.⁴⁷

4.4 | Design variables

For this problem, a relatively flexible design space is created within which the thickness of many of the material stacks can be varied at different regions over the blade span. Some stack definitions remain invariant. For example, the external gelcoat is invariant because it does not play an important role in blade structure and would not be modified for structural purposes. The triax skins, which are thin layers of fiberglass used consistently throughout the blade structure to maintain general structural integrity, are also invariant. Additionally, the thickness of the fiberglass at the root is not modified as it is assumed that the reference thickness is defined to account for the installation of bolts.

Figure 10 identifies the $n_v = 11$ design variables that are used. For a variable indicated by a black numbered marker in the middle of a horizontal line segment, the thickness over the entirety of that line segment is modified by a common variable Δt_i . For a variable indicated by a black marker directly overlapping an inflection point (i.e. variables one and three), the thickness at that inflection point is modified by a variable Δt_i . The connectivity of the linear piecewise functions in Figure 10 remains consistent throughout design variable variation. The variables are illustrated by the expression

$$t_i = t_{\text{ref}_i} + \Delta t_i, \quad i = 1, \dots, n_v, \quad (28)$$

where t_i denotes the thickness at the point or points associated with design variable i for a given optimization iteration, t_{ref_i} denotes the reference thickness of the corresponding point or segment, and Δt_i denotes the value of the design variable for a given optimization iteration.

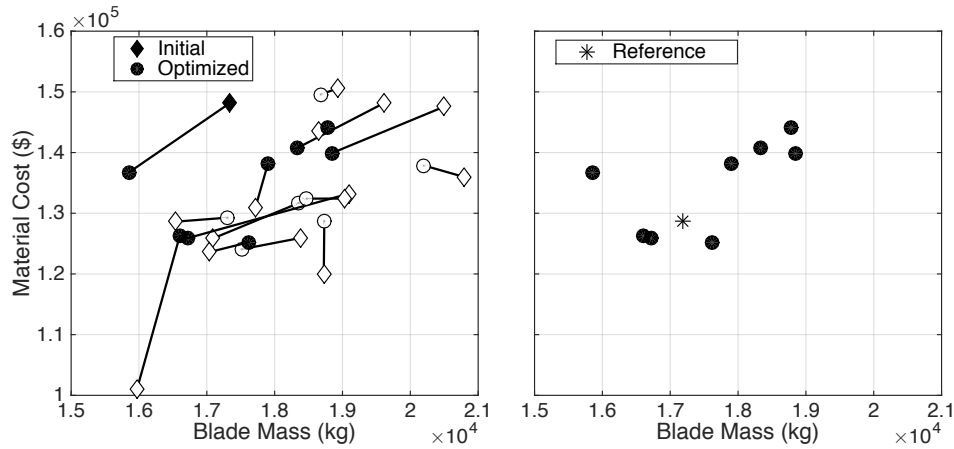


FIGURE 11 At left, blade mass and material cost of each starting point (diamonds) and blade mass and material cost of corresponding optimized designs (circles). Unfilled points signify invalid designs as indicated by an objective function penalization of greater than 0.05. At right, blade mass and material cost of only valid optimized points and reference design.

4.5 | Implementation and solution strategies

The optimization problem represented by Equation 24 is implemented in OpenMDAO,⁶⁰ a python-based software for multidisciplinary design analysis and optimization. FAST-based aeroelastic analyses are performed through the OpenMDAO-based FUSED-Wind⁵⁹; thus, the analyses can be performed in parallel. A similar module is developed to dispatch the two IGA-based buckling analyses in serial from within OpenMDAO. Using this setup, each function evaluation takes approximately 12 minutes on two cores of a Linux machine with Intel Xeon E5-2699 v3 2.30 GHz processors. Each optimization problem is solved using two cores, with clear possibilities for improved efficiency and parallelism in the future. Based on experience, a penalty coefficient of $\beta_i = 1000$ is used for all constraints and the optimization is terminated when the objective function varies by a factor of less than 1.0×10^{-6} .

OpenMDAO provides access to a variety of optimization methods, and gradients can be automatically calculated within OpenMDAO via finite difference. Here, the pyOpt-based⁶⁴ Sequential Least Squares Programming (SLSQP) method is selected for its relative robustness and ability to incorporate gradient information. Experience indicates that the solution space of this particular optimization problem may be quite complicated. While this fact might encourage the use of a global optimization algorithm, global optimization algorithms tend to require large numbers of function evaluations. In this case, each function evaluation is computationally expensive. Thus, instead, multiple gradient-based optimizations are performed with different starting points in the design space. Specifically, Latin hypercube sampling, which has been shown to be more effective than purely random sampling,⁶⁵ is used to generate 15 distinct starting points for the 11 design variables.

4.6 | Results and discussion

The initial mass and total material cost of each sample point as well as the associated optimized mass and total material cost are plotted in Figure 11. The average number of function evaluations for each optimization, including function evaluations required for finite difference gradient evaluation, is approximately 424. A wide variety of optimized designs are generated, and some of the designs do not perform well from a blade mass and material cost perspective. This underscores the value of utilizing many starting points for this particular problem and solution approach. In general, however, one can see that, in the majority of the problems, either mass is decreased, material cost is decreased, the level of constraint violation is decreased, or some combination of these pseudo-objective reduction mechanisms is achieved.

Detailed results of two of the optimizations are given in Table 5, and the values of the corresponding design variables are shown in Figure 12. Each of these optimizations took approximately 2.5 days. The two designs in Table 5 are among the best-performing optimized designs. Both of the designs, according to the objective function, Equation 23, perform better than the baseline 5 MW blade design. However, performance improvement is achieved differently in each case. In the design designated here as the "Balanced" design, both blade mass and material cost are reduced, demonstrating that it is possible to achieve improvement of both blade mass and material cost metrics simultaneously. This balanced design technically performs the best from the perspective of Equation 23. The "Lightweight" design, however, demonstrates improvement only of the blade mass metric, with an accompanying material cost increase. While material cost increase is not desirable from the perspective of the objective function,

TABLE 5 Optimization information and relative performance details of two of the best-performing optimized designs.

Design Name	Initial Objective	Final Objective	Relative Mass (%)	Relative Cost (%)	Function Evaluations
Balanced	1086.29	-0.026	-3.39	-1.80	498
Lightweight	0.08	-0.007	-7.74	+6.32	266

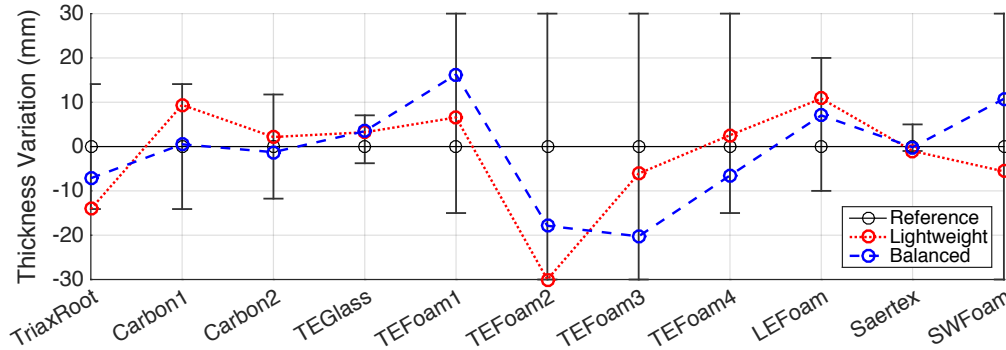


FIGURE 12 Design variable values for the reference, balanced, and lightweight 5 MW blade designs. Bars indicate the allowable range for each design variable.

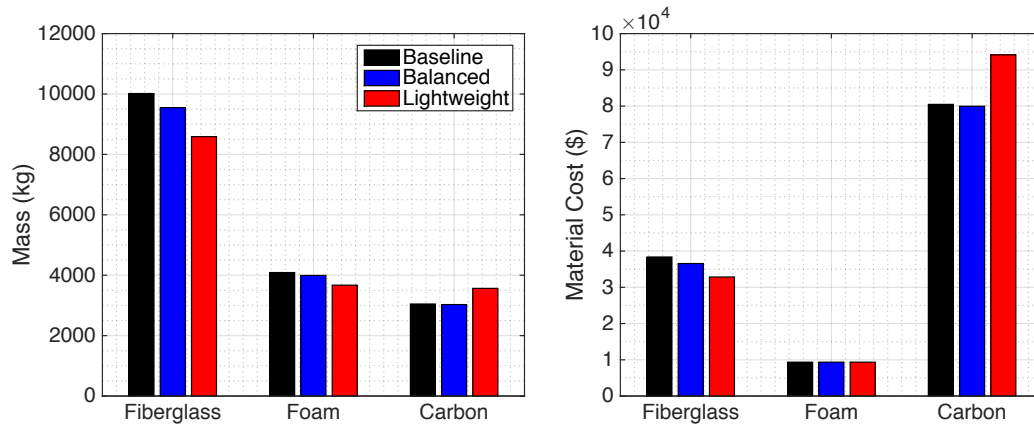


FIGURE 13 The total mass and material cost contributions of the three primary types of materials in the baseline, balanced, and lightweight 5 MW blade designs. Fiberglass includes E-LT-5500, SNL Triax, Saertex, and resin.

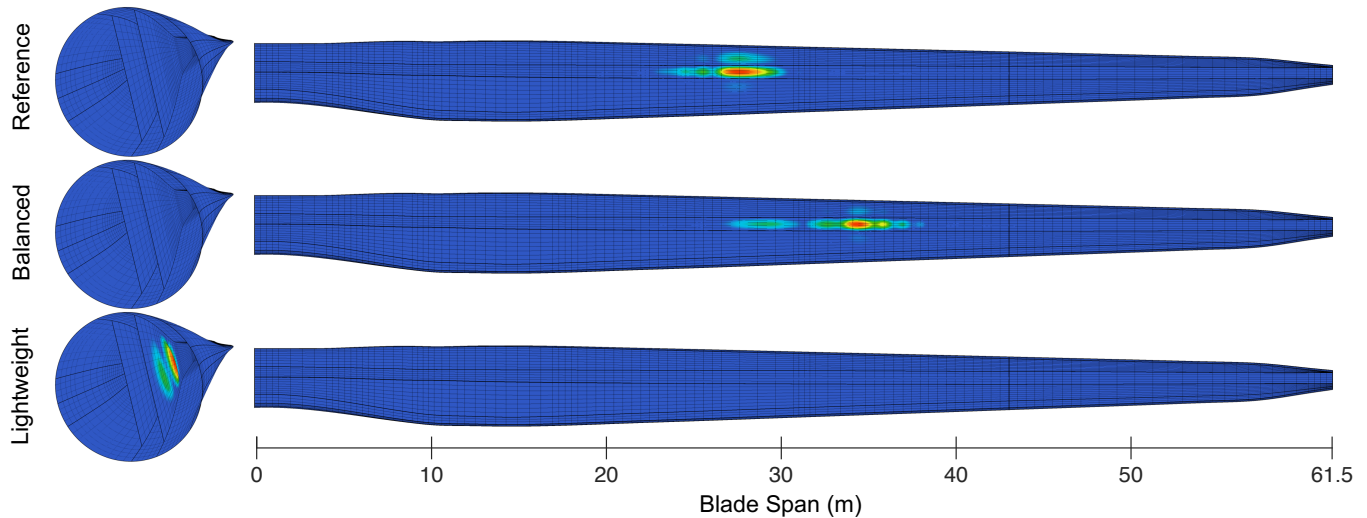
the drastic blade mass reduction of 7.74 % could enable even more cost reduction in downstream components such as the drivetrain or the tower. This could be desirable depending on the design context.

The left side of Figure 13 shows, for the baseline, balanced, and lightweight 5 MW designs, the total mass of the three primary types of materials. The material types are fiberglass, which includes E-LT-5500, SNL Triax, Saertex, and resin; foam; and uni-directional carbon fiber. Similarly, the right side of Figure 13 quantifies the contribution of each type of material towards overall material cost in each of the three designs. For the balanced design, the mass of all three types of materials is reduced relative to the baseline design. In this case, buckling resistance is improved by more optimally distributing fiberglass and foam, as shown in Figure 12. Furthermore, the overall material cost is also reduced in the balanced design because the amount of each type of material is reduced.

The lightweight design demonstrates a substantially different approach. In the lightweight design, the amount of carbon is increased, enabling reductions in the amounts of both fiberglass and foam that are used. Carbon’s high strength-to-weight ratio dictates that this exchange is quite beneficial in terms of blade mass, enabling a 7.74% mass reduction, or over 1300 kg. Due to the high cost of carbon, however, the overall material

TABLE 6 Various performance metrics of the reference and optimized 5 MW blade designs.

Design Name	Mass (kg)	Material Cost (\$)	Buckling % of SF	% Max Deflection	% σ_{UT}
Reference	17 184	128 618	100.41	90.71	37.50
Balanced	16 602	126 300	100.02	92.06	37.10
Lightweight	15 853	136 745	100.01	81.73	47.69

**FIGURE 14** The first buckling mode of the reference (top), balanced (middle), and lightweight (bottom) 5 MW blade designs. Modes are shown in the internal structure of the blade (left) and on the suction side of the blade (right).

cost is adversely affected, even despite the cost reduction stemming from reduced fiberglass usage. Interestingly, the total cost of foam experiences little variation from case to case despite non-zero variables associated with foam thickness. This is because the overall cost that is attributed to foam is dominated by kitting cost, determined by the total area over which the foam is applied, which is invariant in this optimization problem.

The results also illustrate the value of incorporating high-fidelity, IGA-based buckling analysis into an optimization problem like this one. Table 6 shows additional performance details of the reference, balanced, and lightweight designs, including absolute mass, absolute material cost, and relevant constraint values. The buckling load factor for both of the optimized designs is approximately 100% of the design buckling safety factor of 1.62, indicating that the buckling constraint is active. In other words, the 5 MW blade design is governed primarily by buckling in all configurations presented here. If optimization were to be performed without considering this high-fidelity analysis feedback, it is likely that this behavior would not be adequately captured. This could potentially increase the workload in later design stages.

The first buckling mode for the reference, balanced, and lightweight blade designs is shown in Figure 14. In the reference design, buckling occurs in the spar cap at approximately midspan. This result is reasonably consistent with the reference.⁴⁷ In the balanced design, the first buckling mode remains concentrated in the spar cap but is shifted outboard. This is presumably due to the slightly reduced thickness of carbon fiber beyond 22.5 m as a result of a negative “Carbon2” variation as shown in Figure 12. Conversely, the lightweight design shows considerably different buckling behavior, with the first buckling mode concentrated on the inboard region of the shear web nearest to the trailing edge. This is reasonable behavior given the increased thickness of carbon fiber in the spar cap and reduced thickness of both foam and Saertex fiberglass in the shear web.

5 | CONCLUSION

A framework is presented through which IGA-based structural analysis of wind turbine blades can be easily performed. The framework employs the efficient IGA Kirchhoff–Love shell formulation for composites and a penalty coupling technique to accommodate multi-patch geometry construction. The technique is capable of coupling shell interfaces with non-matching control points and discretization, eliminating the restrictive requirements imposed on the geometry construction by other methods.

For the purposes of demonstration, the NREL/SNL 5 MW blade is modeled within Rhinoceros 3D, a NURBS-based CAD modeling software. Analysis-suitable geometries can be generated from a set of input parameters within the CAD software in a matter of seconds, underscoring the seamless approach enabled by IGA. The model behaves comparably to the reference model.⁴⁷ Upon inspecting the behavior of buckling solutions under mesh refinement, it is clear that the IGA-based framework is capable of providing accurate solutions using significantly fewer elements relative to a traditional FEA-based approach.

The NREL/SNL 5 MW blade is also optimized within OpenMDAO⁶⁰ using both FAST and IGA-based buckling analysis. The objective function is defined such that minimization of both blade mass and total material cost are beneficial. Variation of material thickness profiles is enabled through 11 design variables, and constraints are defined based on IEC 61400 requirements. Optimization is performed on 15 initial blade designs, and multiple designs of potential interest are identified. The optimized design with the absolute lowest objective function value, termed the "balanced" design, features both reduced blade mass and reduced material cost relative to the reference design. Alternatively, the "lightweight" design features a significant blade mass reduction of over 7% achieved through the employment of more carbon fiber in the spar cap. In both of these optimizations, the blade's buckling behavior governs the design, highlighting the value of incorporating high-fidelity structural analysis into blade optimization procedures.

The optimization procedure presented here is necessarily limited in scope. If buckling analysis were performed for loads applied over a wider range of load angles, for example, it is quite possible that the results would differ. Additionally, numerous optimization algorithms could be employed, some of which may improve the optimization results. Still, the presented framework provides the means to perform such explorations more easily, more efficiently, and more accurately. It also provides some optimized design alternatives which may perform better than the reference 5 MW design, potentially providing a starting point for future design studies.

ACKNOWLEDGMENTS

A.J. Herrema was supported by the U.S. National Science Foundation (NSF) Grant No. DGE-1069283 which funds the activities of the Integrative Graduate Education and Research Traineeship (IGERT) in Wind Energy Science, Engineering, and Policy (WESEP) at Iowa State University. J. Kiendl was partially supported by the Onsager fellowship program of the Norwegian University of Science and Technology. The authors would like to thank Dr. Baskar Ganapathysubramanian at Iowa State University for suggestions regarding the optimization performed in this work; Dr. Frederik Zahle and Dr. Michael McWilliam, both at Denmark Technical University, for helpful discussions regarding OpenMDAO and multidisciplinary blade design; and Dr. Katherine Dykes at NREL for support and guidance in developing a programmatic wrapper for FAST.

References

1. Manwell JF, McGowan JG, Rogers AL. *Wind Energy Explained: Theory, Design and Application*, 2nd ed. Chichester: John Wiley & Sons; 2009.
2. Money C, Hand M, Bolinger M, Rand J, Heimiller D, Ho J. *2015 Cost of Wind Energy Review*. NREL/TP-6A20-66861: National Renewable Energy Laboratory. Golden, CO; 2017.
3. Cox K, Echtermeyer A. Effects of composite fiber orientation on wind turbine blade buckling resistance. *Wind Energy*. 2014;17(12):1925–1943.
4. Cox K, Echtermeyer A. Structural design and analysis of a 10MW wind turbine blade. *Energy Procedia*. 2012;24:194–201.
5. Chen X, Zhao X, Xu J. Revisiting the structural collapse of a 52.3 m composite wind turbine blade in a full-scale bending test. *Wind Energy*. 2017;17:657–669.
6. Lindgaard E, Lund E. Nonlinear buckling optimization of composite structures. *Computer Methods in Applied Mechanics and Engineering*. 2010;199(37–40):2319–2330.
7. Jensen FM, Weaver PM, Cecchini LS, Stant H, Nielsen RF. The Brazier effect in wind turbine blades and its influence on design. *Wind Energy*. 2012;15(2):319–333.
8. Chehouri A, Younes R, Ilinca A, Perron J. Review of performance optimization techniques applied to wind turbine blades. *Applied Energy*. 2015;142:361–388.
9. Xudong W, Zhu WJ, Sørensen JN, Jin C. Shape optimization of wind turbine blades. *Wind Energy*. 2009;12(8):781–803.
10. Fuglsang P, Madsen HA. Optimization method for wind turbine rotors. *Journal of Wind Engineering and Industrial Aerodynamics*. 1999;80(1–2):191–206.
11. Lanzafame R, Messina M. Fluid dynamics wind turbine design: Critical analysis, optimization and application of BEM theory. *Renewable Energy*. 2007;32(14):2291–2305.

12. Benini E, Toffolo A. Optimal design of horizontal-axis wind turbines using blade-element theory and evolutionary computation. *Journal of Solar Energy Engineering*. 2002;124:357–363.
13. Campobasso MS, Minisci E, Caboni M. Aerodynamic design optimization of wind turbine rotors under geometric uncertainty. *Wind Energy*. 2014;19(1):51–65.
14. Fuglsang P, Bak C, Schepers JG, et al. Site-specific design optimization of wind turbines. *Wind Energy*. 2002;5:261–279.
15. Bottasso CL, Campagnolo F, Croce A, Tibaldi C. Optimization-based study of bend-twist coupled rotor blades for passive and integrated passive/active load alleviation. *Wind Energy*. 2012;16(8):1149–1166.
16. *Wind turbines—Part 1: Design requirements*. IEC 61400-1: International Electrotechnical Commission. Geneva, Switzerland; 2005.
17. Bottasso CL, Campagnolo F, Croce A, Dilli S, Gualdoni F, Nielsen MB. Structural optimization of wind turbine rotor blades by multilevel sectional/multibody/3D-FEM analysis. *Multibody System Dynamics*. 2014;32(1):87–116.
18. Hughes TJR, Cottrell JA, Bazilevs Y. Isogeometric analysis: CAD, finite elements, NURBS, exact geometry and mesh refinement. *Computer Methods in Applied Mechanics and Engineering*. 2005;194:4135–4195.
19. Benson DJ, Bazilevs Y, Hsu M-C, Hughes TJR. A large deformation, rotation-free, isogeometric shell. *Computer Methods in Applied Mechanics and Engineering*. 2011;200:1367–1378.
20. Morganti S, Auricchio F, Benson DJ, et al. Patient-specific isogeometric structural analysis of aortic valve closure. *Computer Methods in Applied Mechanics and Engineering*. 2015;284:508–520.
21. Bazilevs Y, Hsu M-C, Akkerman I, et al. 3D simulation of wind turbine rotors at full scale. Part I: Geometry modeling and aerodynamics. *International Journal for Numerical Methods in Fluids*. 2011;65:207–235.
22. Bazilevs Y, Hsu M-C, Kiendl J, Wüchner R, Bletzinger K-U. 3D simulation of wind turbine rotors at full scale. Part II: Fluid–structure interaction modeling with composite blades. *International Journal for Numerical Methods in Fluids*. 2011;65:236–253.
23. Hsu M-C, Akkerman I, Bazilevs Y. High-performance computing of wind turbine aerodynamics using isogeometric analysis. *Computers & Fluids*. 2011;49:93–100.
24. Bazilevs Y, Hsu M-C, Scott MA. Isogeometric fluid–structure interaction analysis with emphasis on non-matching discretizations, and with application to wind turbines. *Computer Methods in Applied Mechanics and Engineering*. 2012;249–252:28–41.
25. Hsu M-C, Bazilevs Y. Fluid–structure interaction modeling of wind turbines: simulating the full machine. *Computational Mechanics*. 2012;50:821–833.
26. Korobenko A, Hsu M-C, Akkerman I, Tippmann J, Bazilevs Y. Structural mechanics modeling and FSI simulation of wind turbines. *Mathematical Models and Methods in Applied Sciences*. 2013;23(2):249–272.
27. Bazilevs Y, Korobenko A, Deng X, Yan J. Novel structural modeling and mesh moving techniques for advanced fluid–structure interaction simulation of wind turbines. *International Journal for Numerical Methods in Engineering*. 2014;102(3-4):766–783.
28. Bazilevs Y, Deng X, Korobenko A, Scalea F, Todd MD, Taylor SG. Isogeometric fatigue damage prediction in large-scale composite structures driven by dynamic sensor data. *Journal of Applied Mechanics*. 2015;82(9):091008–12.
29. Hsu M-C, Wang C, Herrema AJ, Schillinger D, Ghoshal A, Bazilevs Y. An interactive geometry modeling and parametric design platform for isogeometric analysis. *Computers and Mathematics with Applications*. 2015;70:1481–1500.
30. Yan J, Korobenko A, Deng X, Bazilevs Y. Computational free-surface fluid–structure interaction with application to floating offshore wind turbines. *Computers & Fluids*. 2016;141:155–174.
31. Herrema AJ, Wiese NM, Darling CN, Ganapathysubramanian B, Krishnamurthy A, Hsu M-C. A framework for parametric design optimization using isogeometric analysis. *Computer Methods in Applied Mechanics and Engineering*. 2016;316:944–965.
32. Ferede E, Abdalla MM, Bussel GJW. Isogeometric based framework for aeroelastic wind turbine blade analysis. *Wind Energy*. 2017;20(2):193–210.
33. Bazilevs Y, Calo VM, Cottrell JA, et al. Isogeometric analysis using T-splines. *Computer Methods in Applied Mechanics and Engineering*. 2010;199:229–263.
34. Piegl L, Tiller W. *The NURBS Book (Monographs in Visual Communication)*, 2nd ed. New York: Springer-Verlag; 1997.
35. Benson D. J., Bazilevs Y., De Luycker E., et al. A generalized finite element formulation for arbitrary basis functions: from isogeometric analysis to XFEM. *International Journal for Numerical Methods in Engineering*. 2010;83:765–785.
36. Kiendl J, Bletzinger K-U, Linhard J, Wüchner R. Isogeometric shell analysis with Kirchhoff–Love elements. *Computer Methods in Applied Mechanics and Engineering*. 2009;198:3902–3914.
37. Reddy JN. *Mechanics of Laminated Composite Plates and Shells: Theory and Analysis*, 2nd ed. Boca Raton, FL: CRC Press; 2004.

38. Kiendl J. *Isogeometric analysis and shape optimal design of shell structures*. Lehrstuhl für Statik, Technische Universität München; 2011.
39. Guo Y, Ruess M. Nitsche's method for a coupling of isogeometric thin shells and blended shell structures. *Computer Methods in Applied Mechanics and Engineering*. 2015;284:881–905.
40. Nguyen-Thanh N, Zhou K, Zhuang X, et al. Isogeometric analysis of large-deformation thin shells using RHT-splines for multiple-patch coupling. *Computer Methods in Applied Mechanics and Engineering*. 2017;316:1157–1178.
41. Ruess M, Schillinger D, Bazilevs Y, Varduhn V, Rank E. Weakly enforced essential boundary conditions for NURBS-embedded and trimmed NURBS geometries on the basis of the finite cell method. *International Journal for Numerical Methods in Engineering*. 2013;95:811–846.
42. Ruess M, Schillinger D, Özcan AI, Rank E. Weak coupling for isogeometric analysis of non-matching and trimmed multi-patch geometries. *Computer Methods in Applied Mechanics and Engineering*. 2014;269:46–731.
43. Breitenberger M., Apostolatos A., Philipp B., Wüchner R., Bletzinger K.-U.. Analysis in computer aided design: Nonlinear isogeometric B-Rep analysis of shell structures. *Computer Methods in Applied Mechanics and Engineering*. 2015;284:401–457.
44. Dornisch W, Vitucci G, Klinkel S. The weak substitution method - an application of the mortar method for patch coupling in NURBS-based isogeometric analysis. *International Journal for Numerical Methods in Engineering*. 2015;103(3):205–234.
45. Duong TX, Roohbakhshan F, Sauer RA. A new rotation-free isogeometric thin shell formulation and a corresponding continuity constraint for patch boundaries. *Computer Methods in Applied Mechanics and Engineering*. 2017;316:43–83.
46. Kiendl J, Bazilevs Y, Hsu M-C, Wüchner R, Bletzinger K-U. The bending strip method for isogeometric analysis of Kirchhoff–Love shell structures comprised of multiple patches. *Computer Methods in Applied Mechanics and Engineering*. 2010;199:2403–2416.
47. Resor BR. *Definition of a 5MW/61.5m wind turbine blade reference model*. Technical Report SAND2013-2569: Sandia National Laboratories. Albuquerque, NM; 2013.
48. Jonkman J, Butterfield S, Musial W, Scott G. *Definition of a 5-MW reference wind turbine for offshore system development*. Technical Report NREL/TP-500-38060: National Renewable Energy Laboratory. Golden, CO; 2009.
49. Griffith T, Ashwill TD. *The Sandia 100-meter all-glass baseline wind turbine blade: SNL100-00*. Technical Report SAND2011-3779: Sandia National Laboratories. Albuquerque, New Mexico; 2011.
50. Hernandez V, Roman JE, Vidal V. SLEPc: A Scalable and Flexible Toolkit for the Solution of Eigenvalue Problems. *ACM Trans. Math. Software*. 2005;31(3):351–362.
51. Roman JE, Campos C, Romero E, Tomas A. *SLEPc Users Manual*. DSIC-II/24/02 - Revision 3.7: D. Sistemes Informàtics i Computació, Universitat Politècnica de València. Valencia, Spain; 2016.
52. Balay S, Abhyankar S, Adams MF, et al. *PETSc Users Manual*. ANL-95/11 - Revision 3.7: Argonne National Laboratory. Lemont, IL; 2016.
53. Balay S, Gropp WD, McInnes LC, Smith BF. Efficient management of parallelism in object oriented numerical software libraries. In: Arge E, Bruaset AM, Langtangen HP, eds. *Modern Software Tools in Scientific Computing*, 163–202. Birkhäuser Press; 1997.
54. Felippa CA. *Nonlinear finite element methods*. University of Colorado Boulder, Lecture Notes; 2001.
55. Li XS, Demmel JW. SuperLU_DIST: A scalable distributed-memory sparse direct solver for unsymmetric linear systems. *ACM Trans. Mathematical Software*. 2003;29(2):110–140.
56. ANSYS . <https://www.ansys.com/>. Accessed 27 June 2018.
57. Jonkman J. FAST. National Renewable Energy Laboratory. <https://nwtc.nrel.gov/FAST>; 2015.
58. Larsen TJ. *How 2 HAWC2, the User's Manual*. Risø National Laboratory for Sustainable Energy, Technical University of Denmark. http://orbit.dtu.dk/files/7703110/ris_r_1597.pdf; 2007.
59. Réthoré P-E, Zahle F. *Framework for Unified Systems Engineering and Design of Wind Plants (FUSED-Wind)*. National Renewable Energy Laboratory, Technical University of Denmark. <http://www.fusedwind.org/>; 2017.
60. Gray J, Moore KT, Naylor BA. *OpenMDAO: An open source framework for multidisciplinary analysis and optimization*. 13th AIAA/ISSMO Multidisciplinary Analysis Optimization Conference. <https://arc.aiaa.org/doi/abs/10.2514/6.2010-9101>; 2010.
61. Bir G, Damiani R. *PreComp*. National Renewable Energy Laboratory. <https://nwtc.nrel.gov/PreComp>; 2014.
62. Griffith T, Johanns W. *Large blade manufacturing cost studies using the Sandia blade manufacturing cost tool and Sandia 100-meter blades*. Technical Report SAND2013-2734: Sandia National Laboratories. Albuquerque, NM; 2013.
63. Fletcher R. *Practical Methods of Optimization, 2nd ed*. Chichester: John Wiley & Sons; 1987.
64. Perez RE, Jansen PW, Martins JRRA. pyOpt: A Python-based object-oriented framework for nonlinear constrained optimization. *Structures and Multidisciplinary Optimization*. 2012;45(1):101–118.

65. McKay MD, Beckman RJ, Conover WJ. A comparison of three methods for selecting values of input variables in the analysis of output from a computer code. *Technometrics*. 2000;42:55–61.

How to cite this article: Herrema AJ, Kiendl J, Hsu M-C. A framework for isogeometric-analysis-based design and optimization of wind turbine blade structures. *Wind Energy*. 2019;22:153–170. <https://doi.org/10.1002/we.2276>

APPENDIX

TABLE A1 Definition of cross-sectional parameters used to construct the NREL/SNL 5 MW blade model.^a

Blade span (m)	Airfoil	TE Type	Twist (deg)	Chord (m)	Pitch Axis	DP1	DP2	DP3	DP4	DP5
0.00	circle	round	13.31	3.386	0.5	0.0295	0.4114	0.5886	0.8523	0.9705
0.30 ^c	circle	round	13.31	3.386	0.5	0.0294	0.4114	0.5886	0.8532	0.9706
0.40 ^c	interp	round	13.31	3.386	0.5	0.0293	0.4114	0.5886	0.8535	0.9707
0.50 ^c	interp	round	13.31	3.386	0.5	0.0293	0.4114	0.5886	0.8547	0.9707
0.60 ^c	interp	round	13.31	3.386	0.5	0.0292	0.4114	0.5886	0.8540	0.9708
0.70 ^c	interp	round	13.31	3.386	0.5	0.0291	0.4114	0.5886	0.8543	0.9709
0.80 ^c	interp	round	13.31	3.386	0.5	0.0291	0.4114	0.5886	0.8546	0.9709
1.37	circle	round	13.31	3.386	0.5	0.0288	0.4114	0.5886	0.8562	0.9712
1.50 ^c	interp	round	13.31	3.387	0.4985	0.0287	0.4102	0.5868	0.8565	0.9713
1.60 ^c	interp	round	13.31	3.388	0.4974	0.0286	0.4094	0.5854	0.8568	0.9714
4.10	interp ^b	round	13.31	3.629	0.4692	0.0272	0.3876	0.5508	0.8638	0.9728
5.50	interp	round	13.31	3.873	0.4535	0.0265	0.3755	0.5315	0.8677	0.9735
6.83	interp ^b	flat	13.31	4.124	0.4385	0.0257	0.3639	0.5131	0.8715	0.9743
9.00	interp	flat	13.31	4.461	0.4141	0.0245	0.3450	0.4831	0.8775	0.9755
10.25	DU99-W-405	flat	13.31	4.557	0.4	0.0238	0.3342	0.4658	0.8810	0.9762
12.00	interp	flat	12.53	4.615	0.4	0.0228	0.3313	0.4687	0.8859	0.9772
14.35	DU99-W-350	flat	11.48	4.652	0.4	0.0215	0.3274	0.4726	0.8925	0.9785
17.00	interp	flat	10.68	4.584	0.4	0.0231	0.3230	0.4770	0.8871	0.9769
18.45	interp ^b	flat	10.16	4.506	0.4	0.0240	0.3206	0.4794	0.8841	0.9760
20.50	interp	flat	9.63	4.374	0.4	0.0253	0.3172	0.4828	0.8800	0.9747
22.55	DU97-W-300	flat	9.01	4.249	0.4	0.0265	0.3138	0.4862	0.8758	0.9735
24.60	interp	flat	8.40	4.132	0.4	0.0278	0.3104	0.4896	0.8716	0.9722
26.65	DU91-W-250	flat	7.79	4.007	0.4	0.0291	0.3070	0.4930	0.8674	0.9709
30.75	DU91-W-250	flat	6.54	3.748	0.4	0.0316	0.3003	0.4997	0.8590	0.9684
32.00	interp	flat	6.18	3.672	0.4	0.0323	0.2982	0.5018	0.8565	0.9677
34.85	DU93-W-210	flat	5.36	3.502	0.4	0.0341	0.2935	0.5065	0.8506	0.9659
37.00	interp	flat	4.75	3.373	0.4	0.0354	0.2899	0.5101	0.8462	0.9646
38.95	DU93-W-210	flat	4.19	3.256	0.4	0.0366	0.2867	0.5133	0.8423	0.9634
41.00	interp	sharp	3.66	3.133	0.4	0.0379	0.2833	0.5167	0.8381	0.9621
42.00 ^c	interp	sharp	3.40	3.073	0.4	0.0385	0.2817	0.5183	0.8360	0.9615
43.04 ^d	NACA-64-618	sharp	3.13	3.010	0.4	0.0391	0.2799	0.5201	0.8339	0.9609
45.00	interp	sharp	2.74	2.893	0.4	0.0403	0.2767	0.5233	0.8339	0.9597
47.15	NACA-64-618	sharp	2.32	2.764	0.4	0.0416	0.2731	0.5269	0.8339	0.9584
51.25	NACA-64-618	sharp	1.53	2.518	0.4	0.0442	0.2664	0.5336	0.8339	0.9558
54.67	NACA-64-618	sharp	0.86	2.313	0.4	0.0463	0.2607	0.5393	0.8339	0.9537
57.40	NACA-64-618	sharp	0.37	2.086	0.4	0.0479	0.2562	0.5438	0.8339	0.9521
60.13	NACA-64-618	sharp	0.11	1.419	0.4	0.0705	0.1886	0.6114	0.8339	0.9226
61.50	NACA-64-618	sharp	0.00	1.086	0.4	0.0921	0.1236	0.6764	0.8339	0.9079

Abbreviation: DP, division point

^aRows highlighted in grey indicate cross sections used for aerodynamic analysis. Division points at which a shear web is defined indicated by **boldface**.

^bAn airfoil definition given by Jonkman et al.⁴⁸ was replaced by an interpolated profile for the purposes of smooth geometry.⁴⁷

^cStations that are ignored during IGA model construction in order to achieve more uniform spanwise NURBS discretization.

^dThe spanwise location at which the trailing edge reinforcement terminates.